Materials Advances

ROYAL SOCIETY OF CHEMISTRY

PAPER

View Article Online
View Journal | View Issue

Cite this: *Mater. Adv.*, 2026, 7, 3231

Experimental and computational insights of the new hybrid organic–inorganic compound $(C_6H_9N_2)_2CdI_4$ for advanced optoelectronic applications and biological activities

Arafet Ghoudi,[a] Walid Taouali,[b] José A. Paixão,[c] Noweir Ahmad Alghamdi,[d] Rui Fausto[ef] and Abderrazek Oueslati*[a]

This study reports on the synthesis, structural elucidation, and property investigation of the hybrid organic–inorganic compound $(C_6H_9N_2)_2CdI_4$, which is composed of 2-amino-5-picolinium cations and discrete cadmium tetraiodide anions. The compound was synthesized using a solution-based method, and its crystal structure was determined through single-crystal X-ray diffraction, revealing a triclinic system with the space group $P\bar{1}$. Structural analysis shows that the isolated $[CdI_4]^{2-}$ tetrahedra are embedded within the crystal matrix and stabilized by an extensive hydrogen-bonding network formed with the protonated organic cations. Scanning electron microscopy (SEM) revealed a densely agglomerated morphology characterized by irregularly shaped grains. Raman spectroscopy provided insights into the vibrational characteristics. Optical absorption measurements exhibited a pronounced $\pi \rightarrow \pi^*$ transition at 307 nm, attributed to the aromatic nature of the organic cation, while the absence of low-energy d–d transitions aligns with the closed-shell electronic configuration of Cd^{2+}. Noncovalent interaction analyses based on NCIPLOT and Multiwfn, supported by density functional theory (DFT) calculations, highlighted the key role of hydrogen bonding and van der Waals interactions in stabilizing the crystal lattice and governing molecular packing. Thermal behavior investigated by thermogravimetric and differential scanning calorimetry (TGA/DSC) demonstrated high thermal stability of the compound up to approximately 350 °C. In addition, *in vitro* antioxidant assays revealed significant activity, with DPPH radical scavenging efficiency reaching about 60% at 1 mg ml^{-1} and a strong Fe^{3+} reduction capability, indicating effective electron-donor behavior. These combined experimental and theoretical results establish clear structure–property relationships and suggest that $(C_6H_9N_2)_2CdI_4$ is a promising multifunctional material, offering potential for optoelectronic applications as well as emerging biomedical relevance.

Received 18th January 2026,
Accepted 11th February 2026

DOI: 10.1039/d6ma00080k

rsc.li/materials-advances

I. Introduction

Recent advances in experimental and theoretical methods have deepened the study of noncovalent interactions, which govern self-assembly in supramolecular systems. These interactions, including hydrogen bonding,[1] π–π stacking,[2] van der Waals forces,[3] and electrostatic effects,[3] dictate the formation, stability, and functionality of molecular assemblies across chemistry, biology, and materials science.

Among these, hydrogen bonding remains one of the most widely studied interactions due to its directional nature, relative strength, and selectivity. It is essential in processes such as protein folding, enzyme–substrate binding, DNA base pairing, and crystal engineering.[4–6] The deliberate use of hydrogen bonding has proven invaluable in crystal engineering, host–guest chemistry, and drug design, where precise control over molecular orientation is paramount.[7–9]

[a] *Laboratory for Spectroscopic Characterization and Optics of Materials, Faculty of Sciences, University of Sfax, B. P. 1171, 3000 Sfax, Tunisia. E-mail: oueslatiabderrazek@yahoo.fr*
[b] *Research Laboratory of Asymmetric Synthesis and Molecular Engineering of Materials for Organic Electronic (LR18ES19), Department of Physics, Faculty of Sciences of Monastir, University of Monastir, Avenue of Environment, Monastir, 5019, Tunisia*
[c] *Department of Physics, University of Coimbra, CFisUC, 3004-516 Coimbra, Portugal*
[d] *Departement of Physics, Faculty of Science, Al-Baha University, Alaqiq, 65779, Saudi Arabia*
[e] *Department of Chemistry, University of Coimbra, CQC-IMS, 3004-535 Coimbra, Portugal*
[f] *Spectroscopy@IKU, Department of Physics, Faculty of Sciences and Letters, Istanbul Kultur University, Ataköy Campus, Bakırköy, Istanbul, Turkey*

In this context, class I organic–inorganic hybrid halides, which rely on weak noncovalent forces to connect organic and inorganic units, have emerged as important platforms for developing functional materials. They combine flexible organic moieties with rigid inorganic frameworks, yielding synergistic optical, electronic, and mechanical properties. Consequently, these materials are actively researched for applications in semiconductors, dielectrics, sensors, and photovoltaics.[10,11]

Hybrid compounds containing metal halide frameworks are particularly notable for their tunable electrical conductivity, magnetic ordering, luminescence, and nonlinear optical behavior.[12] Their potential spans diverse fields, including biomedical applications,[13,14] automotive and aerospace industries,[15,16] energy storage,[17] solar energy conversion and LEDs,[18] microelectronics,[19,20] and advanced packaging with barrier or antimicrobial properties.[21]

A key subclass of these materials follows the general formula R_2MX_4, where R is a protonated organic cation, M is a divalent metal cation (*e.g.*, Zn^{2+}, Co^{2+}, Fe^{2+}, Cd^{2+}, ...), and X is a halide ion. These structures typically feature discrete MX_4 tetrahedra stabilized by hydrogen bonding and van der Waals interactions between organic and inorganic components. This structural motif imparts thermal stability and chemical robustness, enabling property modulation through cation or anion substitution.

Among metal halides, halogenocadmates(II) are especially interesting due to the flexible coordination chemistry of Cd^{2+}, which allows diverse structural topologies, from discrete molecular species to extended chains, 2D layers, and 3D networks. This adaptability makes them promising candidates for designing stimuli-responsive materials.[22]

Pyridine-based derivatives hold a prominent position in heterocyclic and medicinal chemistry.[23,24] Their electron-rich aromatic systems and nitrogen lone pairs facilitate coordination and hydrogen bonding. Pyridine and its analogs are widely used in bioactive molecules, metal complex ligands, and supramolecular scaffolds. Incorporating them into hybrid structures often enhances stability, binding selectivity, and supramolecular organization. Notably, 2-amino-5-methylpyridine (2A5MP) is recognized for its versatile binding capabilities due to both amino and nitrogen donor groups. Recent molecular docking studies highlight its potential in target-specific binding, particularly in oncology and enzyme inhibition.[25]

Table 1 summarizes selected hybrid compounds based on 2-amino-5-picoline, illustrating their structural diversity. In all cases, 2-amino-5-picoline serves as the organic component, combined with various divalent metals and halides. The resulting architectures range from discrete units to extended networks, with tunable physical properties that reflect the influence of both metal and halide constituents. Importantly, all reported 2A5MP-based compounds crystallize in centrosymmetric space groups, underscoring their versatility as building blocks for advanced hybrid materials.

This study focuses on $(C_6H_9N_2)_2CdI_4$, a new iodide-based member of the 2A5MP family. The use of iodide extends the chemistry toward heavier, more polarizable halides, enabling a systematic evaluation of halide effects on structure and properties within the same organic framework.

Table 1 Selected hybrid compounds based on 2-amino-5-picoline: chemical formula, crystal system, and space group

Compound	System	Space group	Ref.
$(C_6H_9N_2)_2MnI_4$	Triclinic	$P\bar{1}$	26
$(C_6H_9N_2)_2CoCl_4$	Monoclinic	$P2_1/c$	27
$(C_6H_9N_2)_2MnBr_4$	Triclinic	$P\bar{1}$	28
$(C_6H_9N_2)_2CdCl_4$	Triclinic	$P\bar{1}$	29
$(C_6H_9N_2)FeCl_4$	Monoclinic	$P2_1/c$	30
$(C_6H_9N_2)_2[SbBr_4]Br$	Monoclinic	$C2/m$	31
$(C_6H_9N_2)_2Sb_2I_8$	Triclinic	$P\bar{1}$	32
$(C_6H_9N_2)_2SnCl_6$	Monoclinic	$P2_1/c$	33
$(C_6H_9N_2)_2ZnCl_4$	Monoclinic	$P2_1/c$	34

Beyond optoelectronics, organic–inorganic hybrid halometalates have attracted recent attention for their biological activity, particularly their ability to scavenge reactive oxygen species (ROS). This behavior is often linked to electron or hydrogen donation from organic ligands coordinated to metal–halide frameworks. In the present compound, the electron-rich 2-amino-5-picolinium cation combined with discrete $[CdI_4]^{2-}$ units suggests potential antioxidant functionality. Accordingly, we evaluated the antioxidant properties of $(C_6H_9N_2)_2CdI_4$ using DPPH radical scavenging and ferric reducing power assays, extending the multifunctional relevance of R_2MX_4 hybrids into biomedical applications.

This work adopts an integrated experimental and theoretical approach to elucidate structure–property relationships in $(C_6H_9N_2)_2CdI_4$. Single-crystal X-ray diffraction is combined with Raman and UV-vis spectroscopy, density functional theory (DFT/TD-DFT) calculations, and noncovalent interaction analyses using RDG/NCIPLOT and Multiwfn. This comprehensive strategy reveals how hydrogen bonding and van der Waals interactions govern lattice stability and electronic structure, while highlighting the tunability of optical, thermal, and antioxidant properties through judicious metal and halide selection.

II. Experimental details

1. Synthesis and single-crystal X-ray characterization of $(C_6H_9N_2)_2CdI_4$

The hybrid compound $(C_6H_9N_2)_2CdI_4$ was synthesized using a slow evaporation method, designed to promote the growth of well-defined single crystals. The detailed procedure is illustrated in Fig. 1. First, 0.1 g of cadmium iodide (CdI_2) was dissolved in 5 ml of hydroiodic acid (HI)-acidified distilled water under gentle stirring. Separately, 0.059 g of 2-amino-5-picoline ($C_6H_8N_2$) was dissolved in 5 ml of the same solvent. Both solutions were stirred until completely clear, indicating full dissolution of all components.

The two solutions were then combined under continuous stirring for 5 minutes, followed by the addition of 2–3 drops of concentrated HI to maintain an acidic environment. The resulting mixture was stirred for an additional 15 minutes at room

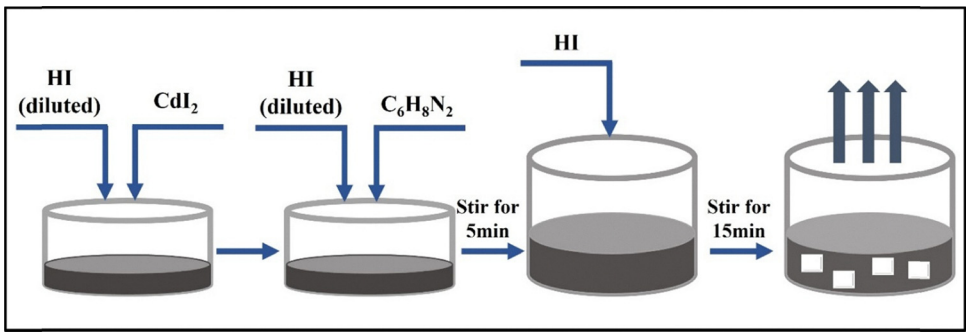

Fig. 1 Schematic diagram for the synthesis process of $(C_6H_9N_2)_2CdI_4$.

temperature to ensure complete homogenization. The solution was then allowed to stand undisturbed at ambient temperature for several days, during which yellow plate-like single crystals formed due to slow solvent evaporation and controlled supersaturation.

The overall chemical reaction can be represented as:

$$2(C_6H_9N_2) + CdI_2 + 2HI \rightarrow (C_6H_9N_2)_2CdI_4 \quad (1)$$

A well-formed single crystal of $(C_6H_9N_2)_2CdI_4$, measuring 0.29 × 0.145 × 0.100 mm^3, was selected using a polarizing microscope and mounted on a Bruker APEX II four-circle area detector diffractometer. X-ray diffraction data were collected at 296(2) K using Mo Kα radiation (λ = 0.71073 Å), monochromated with a graphite crystal. Data acquisition was performed using the APEX2 software suite.[35] The reflections were measured within a 2θ range of 2.580° to 27.493°, and empirical absorption corrections were applied using the SADABS program,[36] based on a multi-scan analysis. The crystal structure was solved by direct methods using SHELXT-2018, which enabled the localization of heavy atoms. Subsequent refinement of the structure and determination of lighter atom positions were carried out with SHELXL-2014, both included in the WINGX software package.[37] A summary of the experimental conditions and refinement parameters is provided in Table 2.

CCDC 2284327 contains the supplementary crystallographic data for $(C_6H_9N_2)_2CdI_4$.

Table 2 Crystallographic data and structure refinements of $(C_6H_9N_2)_2CdI_4$

Formula	$(C_6H_9N_2)_2CdI_4$
Color/shape	Yellow/platelets
Formula weight ($gmol^{-1}$)	838.30
Crystal system	Triclinic
Space group	$P\bar{1}$
Density	2.481
Crystal size (mm)	0.29 × 0.145 × 0.100
Temperature (K)	296(2)
Diffractometer	Bruker APEXII
a (Å)	8.541(2)
b (Å)	9.446(2)
c (Å)	15.217(4)
α (°)	83.619(12)
β (°)	89.011(13)
γ (°)	66.923(11)
V ($Å^3$)	1122.0(5)
Z	2
Radiation type	Mo Kα (0.71073 Å)
Absorption correction	Multi-scan
θ range for data collection (°)	2.580 ≤ θ ≤ 27.493
Measured reflections	31 347
Independent reflections	5127
Observed data [$I > 2\sigma(I)$]	4252
Index ranges	$h = -11 \rightarrow 11$
	$k = -12 \rightarrow 12$
	$l = -19 \rightarrow 19$
F(000)	756
Number of parameters	192
R_1	0.0271
wR_2	0.0675
Goof	1.093

2. Crystal morphology, thermal stability, and spectroscopy (Raman, UV-visible) analyses: instrumentation and procedures

The crystal's surface morphology was investigated using a TESCAN Vega III scanning electron microscope (SEM). Elemental composition was analyzed through energy-dispersive X-ray spectroscopy (EDX), utilizing the Bruker Quantax 100 Easy EDX system. This system is equipped with a Bruker XFlash 410 M Silicon Drift Detector, offering a high energy resolution of 133 eV for Mn Kα at 100 kcps. The EDX setup is fully integrated into the SEM platform, enabling precise and efficient compositional analysis.

The thermal stability and mass variation of the samples were investigated using a PerkinElmer STA6000 differential scanning calorimeter under a controlled nitrogen environment. The analyses were performed with a uniform heating rate of 10 °C min^{-1}, during which the responses of the specimen and the reference were recorded concurrently.

Raman spectra were recorded using a Horiba LabRam HR Evolution Raman microscope, equipped with a 633 nm excitation laser operating at an approximate power of 50 mW at the sample surface. A 100× objective lens was utilized to focus the laser to a spot size of about 1 μm, ensuring high spatial resolution. Instrument calibration was performed using a silicon reference crystal, with the characteristic Raman band set at 520.5 cm^{-1}. Each final spectrum represents the average of 10 successive acquisitions, each with an integration time of 5 seconds, to enhance signal-to-noise ratio and ensure spectral reliability.

UV-visible absorption measurements were carried out using a HITACHI U-3300 spectrophotometer (both in absorbance and

reflectance modes, slit width of 20 nm, and LISR-3100 integrated sphere; $BaSO_4$ was used as a reference), covering the spectral range from 250 to 400 nm.

3. Determination of *in vitro* antioxidant activities

3.1. DPPH radical scavenging activity. The free radical-scavenging potential of the $(C_6H_9N_2)_2CdI_4$ compound was evaluated following the method of Bersuder *et al.*[38] In brief, 500 µl of the sample at various concentrations (0.05–1 mg ml^{-1}) was combined with 375 µl of ethanol (99.5%) and 125 µl of DPPH solution (0.02% in ethanol, 99.5%). The resulting mixtures were incubated at room temperature in the dark for 1 hour. After incubation, the absorbance was measured at 517 nm using a UV-visible spectrophotometer. The DPPH radical scavenging percentage was calculated as:

$$\text{Scavenging activity } (\%) = \frac{A_c - A_s}{A_c} \times 100$$

where A_c represents the absorbance of the control solution and A_s is the absorbance of the sample mixed with DPPH. Vitamin C was used as the positive control.

3.2. Reducing power assay. The iron(III) reducing capacity of $(C_6H_9N_2)_2CdI_4$ was evaluated following the method of Yildirim *et al.*[39] In brief, 1 ml of the sample at various concentrations (0.05–1 mg ml^{-1}) was combined with 1.25 ml of phosphate buffer (0.2 M, pH 6.6) and 2.5 ml of 1% (w/v) potassium ferricyanide solution. The mixture was incubated at 50 °C for 20 minutes to allow reduction of Fe^{3+}. Subsequently, 2.5 ml of 10% (w/v) trichloroacetic acid was added to stop the reaction, and the samples were centrifuged at 10 000 × *g* for 10 minutes. From the resulting supernatant, 2.5 ml was mixed with 2.5 ml of distilled water and 0.5 ml of 0.1% (w/v) ferric chloride solution. The absorbance of the resulting solution was measured at 700 nm using a UV-visible spectrophotometer. Vitamin C was employed as the reference standard.

III. Results and discussion

1. Structure description

In a previous study,[29] the hybrid compound $(C_6H_9N_2)_2CdCl_4$ was successfully synthesized and structurally characterized. It crystallizes at room temperature in the triclinic crystal system, adopting the centrosymmetric space group $P\bar{1}$. The refined unit cell parameters are: a = 7.7127(3) Å, b = 8.6907(3) Å, c = 15.0834(5) Å, α = 94.472(2)°, β = 91.016(2)°, γ = 111.725(1)°, with a unit cell volume of V = 935.16(6) $Å^3$. The crystal structure consists of isolated $[CdCl_4]^{2-}$ tetrahedra, each charge-compensated by two protonated 2-amino-5-picolinium $(C_6H_9N_2)^+$ cations. These units are interconnected *via* hydrogen bonding and weak intermolecular interactions, contributing to the cohesion of the lattice.

In the present investigation, a structural change was observed upon halide substitution, where chloride ions were replaced by iodide ions to yield the new compound $(C_6H_9N_2)_2CdI_4$ under investigation. Remarkably, this iodide-based compound retains the same triclinic crystal system and $P\bar{1}$ space group. However, due to the significantly larger ionic radius and higher polarizability of I^- compared to Cl^-, notable changes in the unit cell dimensions were observed. As listed in Table 2, the refined parameters are: a = 8.541(2) Å, b = 9.446(2) Å, c = 15.217(4) Å, α = 83.619(12)°, β = 89.011(13)°, γ = 66.923(11)°, with a unit cell volume of V = 1122.0(5) $Å^3$ and Z = 2. This expansion reflects the influence of iodide on the molecular packing and overall structural framework.

The asymmetric unit (Fig. 2) contains discrete $[CdI_4]^{2-}$ tetrahedra, where Cd^{2+} is coordinated to four iodide ligands. Each anion is surrounded by two $(C_6H_9N_2)^+$ cations, forming a dense hydrogen-bonding network *via* N–H···I contacts. π···π stacking between adjacent pyridine rings further stabilizes the packing, leading to a three-dimensional supramolecular framework.

To better understand the crystalline architecture, a structural projection along the crystallographic *a*-axis is shown in Fig. 3. This view reveals a regular alternation of cationic and anionic layers parallel to the (001) plane.

The anionic moiety $[CdI_4]^{2-}$ exhibits a distorted tetrahedral geometry. The Cd–I bond lengths range between 2.7461(8) Å and 2.8130(8) Å, while the I–Cd–I bond angles vary from 105.00(2)° to 116.69(2)° (Table 3). These values are consistent with the reported $[CdI_4]^{2-}$ structure.[8,40]

To quantify the tetrahedral distortion, the Baur distortion index was calculated:[41]

$$\text{DI(Cd–I)} = \sum_{i=1}^{n_1} \frac{|d_i - d_m|}{n_1\, d_m};$$
$$\text{DI(I–Cd–I)} = \sum_{i=1}^{n_2} \frac{|a_i - a_m|}{n_2 a_m}; \quad (2)$$

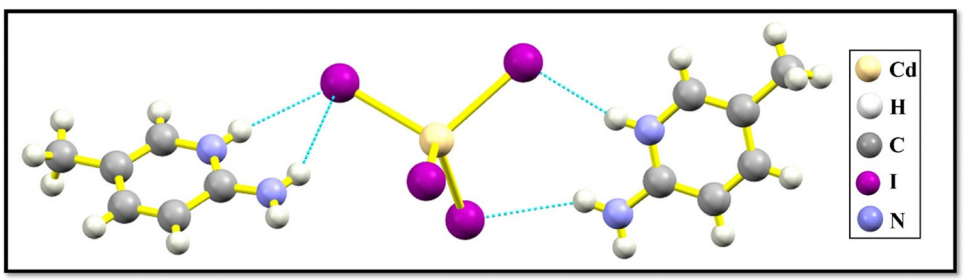

Fig. 2 The asymmetric unit of $(C_6H_9N_2)_2CdI_4$. Dashed lines represent hydrogen bonds.

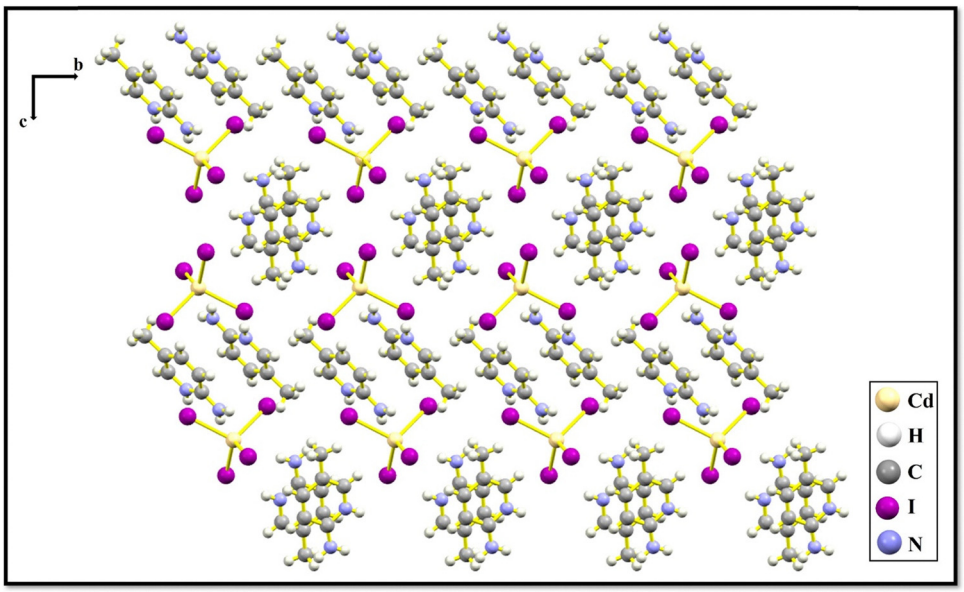

Fig. 3 Projection of the structure of $(C_6H_9N_2)_2CdI_4$ along the crystallographic *a*-axis.

Table 3 Selected bond distances (Å) and angles (°)

Distances (Å)		Angles (°)	
Cd1–I1	2.7461(8)	I1–Cd1–I2	112.91(2)
Cd1–I2	2.7980(7)	I1–Cd1–I3	116.69(2)
Cd1–I3	2.7600(8)	I1–Cd1–I4	105.00(2)
Cd1–I4	2.8130(8)	I2–Cd1–I3	105.31(1)
N1–C2	1.367(8)	I2–Cd1–I4	109.61(2)
N1–C6	1.326(6)	I3–Cd1–I4	107.12(2)
C1–C3	1.508(9)	C2–N1–C6	123.4(5)
C2–C3	1.350(9)	C1–C3–C2	121.1(6)
C3–C4	1.402(7)	C1–C3–C4	122.5(6)
C4–C5	1.340(9)	C2–C3–C4	116.4(5)
C5–C6	1.388(8)	C3–C4–C5	121.9(6)
C6–N2	1.343(7)	C4–C5–C6	120.5(5)
C7–C9	1.492(9)	N1–C6–C5	117.1(5)
N3–C8	1.342(8)	N1–C6–N2	119.7(5)
N3–C12	1.332(6)	C5–C6–N2	123.2(5)
C8–C9	1.359(8)	C8–N3–C12	124.3(5)
C9–C10	1.392(6)	N3–C8–C9	121.3(5)
C10–C11	1.341(9)	C7–C9–C8	121.6(5)
C11–C12	1.419(8)	C7–C9–C10	122.5(5)
C12–N4	1.330(8)	C8–C9–C10	115.9(5)
		C9–C10–C11	122.8(5)
		C10–C11–C12	119.7(5)
		N3–C12–C11	115.9(5)
		N3–C12–N4	120.2(5)
		C11–C12–N4	123.9(5)

where, d = Cd–I distance, a = I–Cd–I angle, m = average value, n_1 = 4 and n_2 = 6 for tetrahedral environment.

The calculated distortion indices, DI(Cd–I) = 0.0094 and DI(I–Cd–I) = 0.0332, suggest that the $[CdI_4]^{2-}$ unit deviates slightly from an ideal tetrahedral configuration, where all bond lengths and angles would be identical (*i.e.*, ~109.5° and equivalent Cd–I distances). The small yet noticeable deviation in both bond lengths and angles indicates that the tetrahedron is subtly distorted. This distortion arises mainly due to intermolecular interactions, particularly N–H···I hydrogen bonds formed between the $[CdI_4]^{2-}$ anion and the surrounding $(C_6H_9N_2)^+$ cations.

The $[CdI_4]^{2-}$ anionic unit can theoretically adopt several geometries, such as tetrahedral, square planar, or seesaw configurations. To determine the actual geometry of the cadmium-centered polyhedron in the present compound, we employed the distortion index τ_4, which quantifies the deviation from ideal geometries. This parameter ranges from 0 for a perfect square planar shape to 1 for a perfect tetrahedron. It is calculated using the following formula:[42]

$$\tau_4 = \frac{360 - (\alpha + \beta)}{360 - 2\theta} \quad (3)$$

where α and β are the two largest bond angles within the coordination polyhedron, and θ is the ideal tetrahedral angle (109.5°). For the $[CdI_4]^{2-}$ unit, using α = 89.011° and β = 83.619°, the τ_4 value is calculated as 0.957. This τ_4 value, very close to 1, clearly indicates that the $[CdI_4]^{2-}$ unit adopts an almost ideal tetrahedral geometry.

The geometric parameters of the protonated amine cations, summarized in Table 3, are consistent with those observed in similar cadmium-based hybrid structures.[29] The overall structural cohesion is primarily maintained through N–H···I hydrogen bonding interactions between the organic cations and the $[CdI_4]^{2-}$ tetraiodocadmate(II) anions, as well as π···π stacking interactions between the aromatic systems of neighboring organic moieties.

Each $(C_6H_9N_2)^+$ cation participates in multiple hydrogen bonding interactions with three distinct $[CdI_4]^{2-}$ anions, as depicted in Fig. 4(a). Conversely, each $[CdI_4]^{2-}$ tetrahedron is stabilized by six hydrogen bonds formed with adjacent organic cations (Fig. 4(b)). The distances between nitrogen and iodine atoms involved in hydrogen bonding (N···I) span from 3.545 to 3.807 Å, while the corresponding N–H···I bond angles range

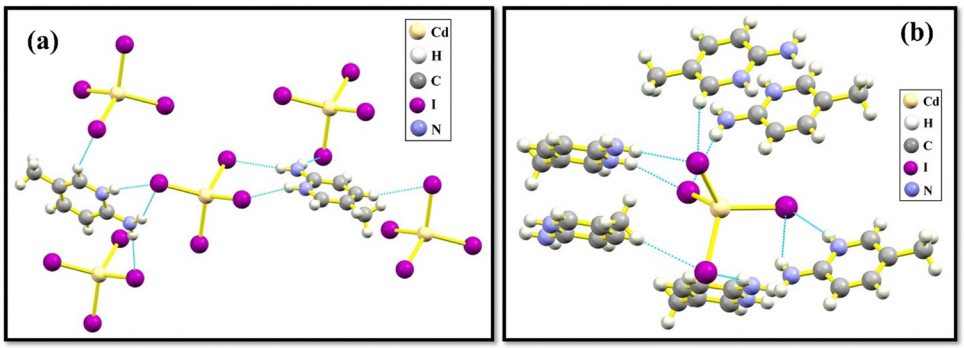

Fig. 4 Hydrogen bonds established by (a) the protonated amine and (b) the metallic tetrahedron in $(C_6H_9N_2)_2CdI_4$.

Table 4 Hydrogen bonding geometry (Å, °)

D—H···A	D—H	H···A	D···A	D—H···A
N2–H2B···I2[a]	0.86	2.919	3.765	168.22
N2–H2A···I1	0.86	2.932	3.703	150.12
N1–H1···I4	0.859	2.73	3.545	159.01
N3–H3A···I3	0.86	2.754	3.602	169.32
N4–H9···I4[b]	0.86	2.954	3.807	171.54

[a] 1 + *x*, *y*, *z*. [b] *x*, 1 + *y*, *z*.

from 150.12° to 171.54°, reflecting the directional nature and varying strengths of these interactions (Table 4).

In addition to hydrogen bonding, π···π stacking interactions are present, adopting a parallel-displaced configuration between their aromatic rings, commonly observed in such supramolecular assemblies.[43,44] The shortest centroid-to-plane distance between two adjacent aromatic rings is measured at 3.882 Å, which falls within the typical range for effective π···π interactions, contributing further to the stability and packing of the crystal lattice.

2. SEM/EDX results

Scanning electron microscopy (SEM) images at increasing magnifications (100×, 1000×, 5000×) reveal a densely agglomerated microstructure composed of irregular polyhedral grains with rough, compact surfaces (Fig. 5), suggesting strong intergranular adhesion.

Complementary EDX analysis, presented in Fig. 6, was conducted to verify the elemental composition and spatial distribution of constituent atoms. The EDX spectrum in Fig. 6(a) confirms the presence of carbon (C), nitrogen (N), cadmium (Cd), and iodine (I), as expected based on the molecular formula. Notably, no additional peaks were detected, indicating the absence of impurities. As is commonly known, hydrogen atoms are not detectable *via* EDX due to their low atomic number and lack of significant X-ray emission.[45]

Fig. 6(b)–(f) show the elemental mapping results, which demonstrate a homogeneous distribution of all detected elements across the sample surface on the micrometer scale. This uniform elemental distribution corroborates the compositional purity of the synthesized hybrid material and supports the consistency of its crystal structure.

3. Thermal stability evaluation

Differential scanning calorimetry (DSC) and thermogravimetric analysis (TGA) of $(C_6H_9N_2)_2CdI_4$ were carried out in the 50–450 °C temperature range at a heating rate of 10 °C min^{-1} under nitrogen. The corresponding curves are presented in Fig. 7. The sample shows a nearly constant mass and an almost featureless DSC baseline up to about 350 °C, indicating the absence of phase transitions or significant degradation in this interval and confirming a wide stability window for the title compound. Above this temperature, a sharp endothermic event is observed in the DSC trace, accompanied by a steep weight loss in the TGA curve, which can be ascribed to the onset of irreversible thermal decomposition of $(C_6H_9N_2)_2CdI_4$.

4. Vibrational analysis

The room-temperature Raman spectrum of the synthesized compound is presented in Fig. 8. The vibrational mode assignments, listed in Table 5, were made by comparison with reported spectra of structurally related compounds.[8,27,29,46–50]

In the low-frequency region (below 400 cm^{-1}), the observed Raman bands are primarily associated with vibrational motions of the inorganic $[CdI_4]^{2-}$ tetrahedral units. Specifically, the peaks appearing at 118 cm^{-1} and 147 cm^{-1} correspond to the symmetric and asymmetric Cd–I stretching modes, respectively. These values are consistent with those reported for other tetrahedral Cd^{2+} complexes containing iodide ligands.[8,47,48] Additionally, the bands located at 54 cm^{-1} and 110 cm^{-1} can be attributed to I–Cd–I bending modes, reflecting the internal flexibility of the $[CdI_4]^{2-}$ framework.

In the mid and high frequency regions (above 400 cm^{-1}), the Raman spectrum is dominated by vibrational modes of the organic $(C_6H_9N_2)^+$ cation. The rocking vibration of the methyl group (γCH_3) is observed at 725 cm^{-1}. The amino group rocking (γNH_2) and wagging (wNH_2) modes are identified at 1155 cm^{-1} and 645 cm^{-1}, respectively. Vibrational modes involving the C–N–C moiety within the aromatic ring are also observed experimentally: the antisymmetric and symmetric CNC stretching modes (νCNC) appear at 1344 cm^{-1}, while the exocyclic C–N stretching mode ($\nu C–N$) is located at 1234 cm^{-1}. The methyl group deformation vibrations are seen at 1386 cm^{-1} (symmetric bending mode) and 1410 cm^{-1} (antisymmetric

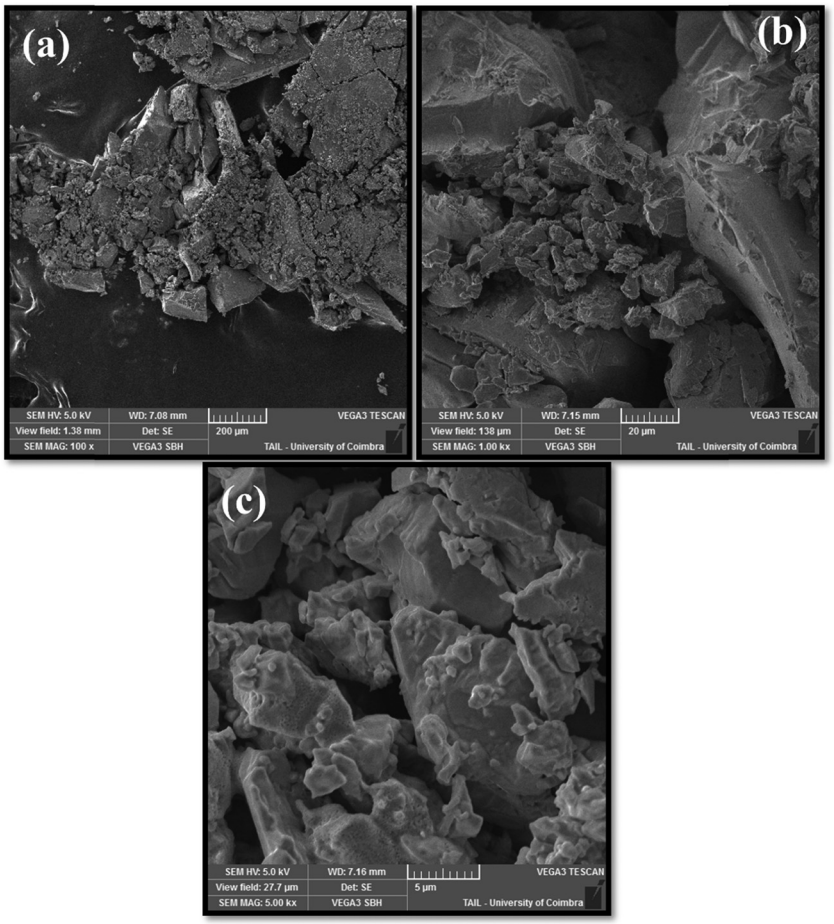

Fig. 5 Scanning electron microscopy images of $(C_6H_9N_2)_2CdI_4$ at different magnifications: (a) 100×, (b) 1000×, and (c) 5000×.

modes). The δNH_2 scissoring and in-plane N–H bending (δN–H) vibrations are detected at 1662 cm^{-1} and 1620 cm^{-1}, respectively. These assignments are consistent with those typically reported for protonated aminopyridine derivatives.[27,29,50]

In the high wavenumber range, the spectrum exhibits bands related to C–H stretching modes of the methyl group at 2863 cm^{-1} and 2919 cm^{-1} (symmetric stretching), and at 2960 cm^{-1} (antisymmetric stretching). The aromatic C–H stretching vibrations appear in their expected spectral region, spanning 3024 to 3145 cm^{-1}. Notably, broad and low intensity features centered at 3652, 3312, and 3196 cm^{-1} are attributed to N–H stretching vibrations, including both symmetric and antisymmetric νNH_2 modes and the νN–H ring stretches. The broadening of these bands indicates that the amino and ring N–H groups are involved in strong hydrogen bonding, in agreement with the crystallographic data.

As a whole, the observed vibrational spectrum aligns well with those expected for the $[CdI_4]^{2-}$ anion and $(C_6H_9N_2)^+$ cation.

5. Optoelectronic properties of $(C_6H_9N_2)_2CdI_4$ compound

The UV-visible absorption spectrum of the hybrid compound $(C_6H_9N_2)_2CdI_4$, shown in Fig. 9, displays a distinct and intense absorption band centered at 307 nm. This band is assigned to a $\pi \rightarrow \pi^*$ transition, attributed to the aromatic moiety of the 2-amino-5-methylpyridinium cation.[29] Such transitions are characteristic of organic chromophores with conjugated π-electron systems and significantly contribute to light-harvesting efficiency in hybrid architectures.[51] In general, organic–inorganic halometalates of formula $(C_6H_9N_2)_2MX_4$, where $[MX_4]^{2-}$ represents a tetrahedral metal halide anion, exhibit composite absorption features. The organic π-system dominates absorption in the UV region, while the metal-halide unit contributes through charge-transfer (CT) or d–d transitions depending on the nature of M. For example, $(C_6H_9N_2)_2CoCl_4$ exhibits strong $\pi \rightarrow \pi^*$ bands in the range of 200–400 nm, in addition to charge-transfer and d–d transitions extending up to 800 nm.[27] In contrast, $(C_6H_9N_2)_2CdCl_4$, incorporating the d^{10} closed-shell Cd^{2+} ion, lacks low-energy d–d transitions and exhibits only a strong $\pi \rightarrow \pi^*$ absorption,[29] leading to a sharper and more distinct band edge.

To evaluate the optical bandgap (E_g), a key parameter in determining a material's suitability for optoelectronic applications such as UV photodetectors, light-emitting diodes, or dielectric insulators,[52–54] the absorption coefficient (α) was extracted using the Beer–Lambert relation

$$\alpha = \frac{2.303 \times A}{l} \quad (4)$$

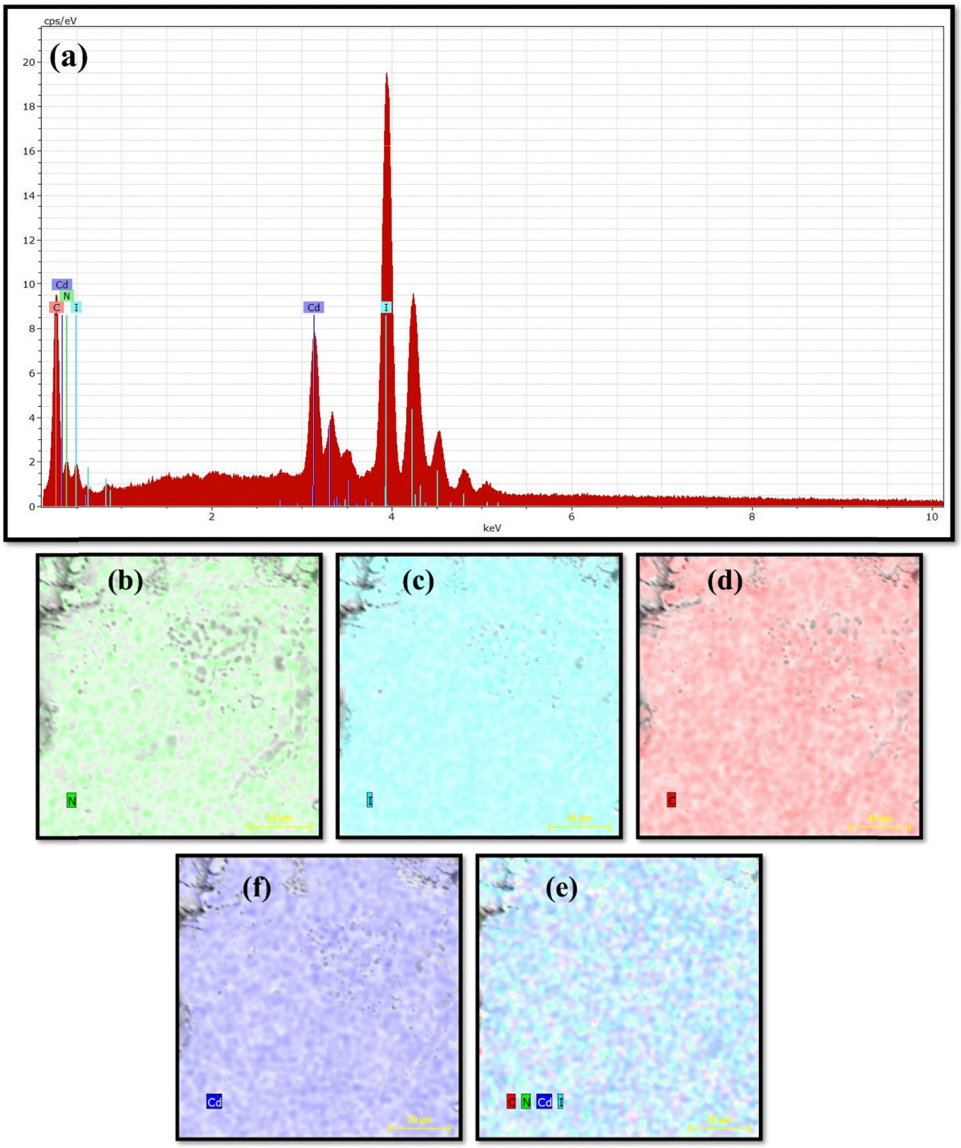

Fig. 6 (a) EDX spectrum of the synthesized $(C_6H_9N_2)_2CdI_4$ material, and (b)–(f) EDX element distribution charts.

where A is the absorbance and l is the sample thickness. The nature of the transition was then deduced using the Tauc formalism:

$$(\alpha h\nu)^{1/n} = \beta(h\nu - E_g) \quad (5)$$

where n is the exponent indicating the type of transition ($n = 1/2$ for direct and $n = 2$ for indirect transition), and β is a constant related to disorder.

Among the tested models, the most accurate and well-fitted plot corresponds to $n = 1/2$, obtained by plotting $(\alpha h\nu)^2$ *versus* photon energy ($h\nu$). This result aligns with the Tauc model, confirming that the compound exhibits a direct allowed electronic transition. Plotting $(\alpha h\nu)^2$ *versus* photon energy ($h\nu$) yields a linear region, whose extrapolation to $((\alpha h\nu)^2 = 0)$ (Fig. 10) gives the direct bandgap E_g = 3.76 eV for $(C_6H_9N_2)_2CdI_4$. This value is slightly higher than the 3.43 eV gap observed for its chlorinated analogue $(C_6H_9N_2)_2CdCl_4$,[29] suggesting that despite iodide's greater polarizability and ionic radius,[26,55,56] factors that generally narrow the bandgap, the extended Cd–I bonds and reduced orbital overlap in $[CdI_4]^{2-}$ may elevate the conduction band minimum or depress the valence band maximum, thereby widening E_g. Additional structural factors such as hydrogen bonding, anion polarizability, and crystalline packing also influence the electronic landscape of these materials.[57,58]

A broader comparison across various $(C_6H_9N_2)_2MX_4$ compounds further emphasizes the tunability of optical properties *via* metal and halide substitution. For example, transition metals with partially filled d-orbitals, such as Mn^{2+} (d^5), Fe^{2+} (d^6), and Co^{2+} (d^7), introduce low-energy d–d transitions and mid-gap states that significantly reduce E_g, as evidenced by values ranging from 2.21[26] to 2.47 eV[30] for Mn and Fe-based chlorides. Conversely, closed-shell d^{10} cations like Cd^{2+} exhibit wider gaps (3.43–3.76 eV) due to the absence of such

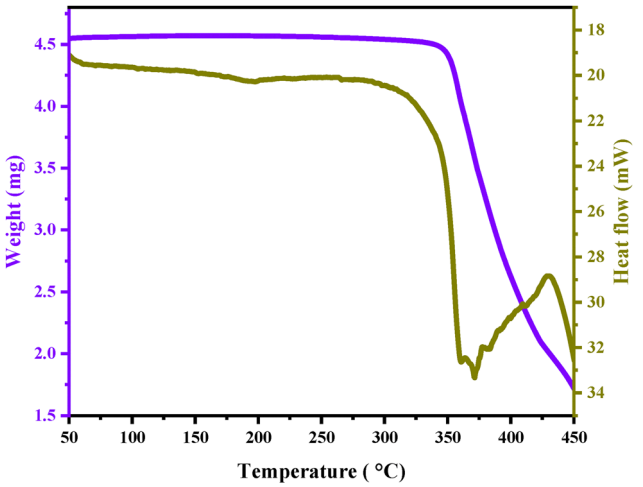

Fig. 7 Thermogravimetric analysis (TGA) and differential scanning calorimetry (DSC) curves of $(C_6H_9N_2)_2CdI_4$.

transitions. Furthermore, halide substitution affects E_g through changes in ionic size and orbital character:[59,60] replacing Cl^- with Br^- or I^- generally increases the valence-band energy due to the higher energy and polarizability of the heavier halides; however, this does not always translate to a smaller bandgap, as structural and orbital interactions modulate the outcome.[61,62] As summarized in Table 6, these variations enable precise optical tuning across the UV-visible spectrum. Overall, the $(C_6H_9N_2)_2CdI_4$ compound, with its high bandgap, direct transition, and sharp $\pi \rightarrow \pi^*$ absorption edge, represents a compelling candidate for wide-bandgap optoelectronic applications, while also highlighting the structural versatility and design flexibility of organic–inorganic halometalates.

Table 5 Observed Raman frequencies (cm^{-1}) and band assignments for $(C_6H_9N_2)_2CdI_4$

Raman shift (cm^{-1})	Assignment
3312	νNH_2 as.
3265	νNH_2 s.
3196	νN–H
3145–3024	νCH ring
2955	νCH_3 as.
2863/2919	νCH_3 s.
1662	δNH_2
1620	δN–H
1548–1460	νCC ring as.; δCH ring
1410	δCH_3 as.
1386	δCH_3 s.
1344	νCNC as. ring
1320	δCH ring
1234	$\nu C–N(H_2)$
1155	γNH_2
987	γCH ring
854	$\nu C–C(H_3)$
792	γN–H
757	δCCC ring
723	γCH_3
645	wNH_2
305–480	Ring deformations and torsions
147	νCdI as.
118	νCdI s.
110	δI–Cd–I as.
54	δI–Cd–I s.

ν, stretching; δ, bending; γ, rocking; w, wagging; s., symmetric; as., antisymmetric.

To better understand the optoelectronic properties of the $(C_6H_9N_2)_2CdI_4$ compound and to explain the experimental results, time-dependent density functional theory (TD-DFT) simulations were carried out. GaussView 5[63] was utilized to prepare input files and to visualize different computed results.

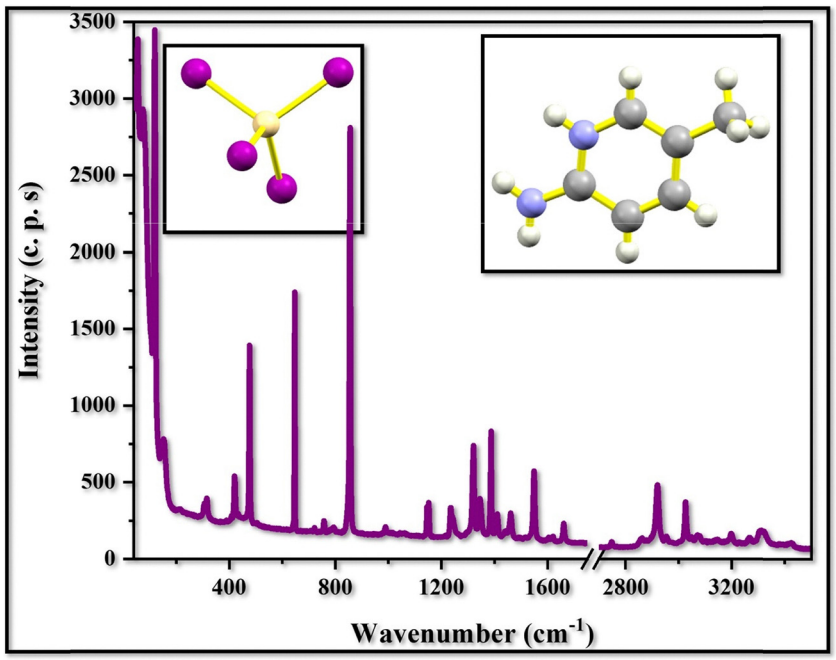

Fig. 8 Raman spectrum of $(C_6H_9N_2)_2CdI_4$ at room temperature.

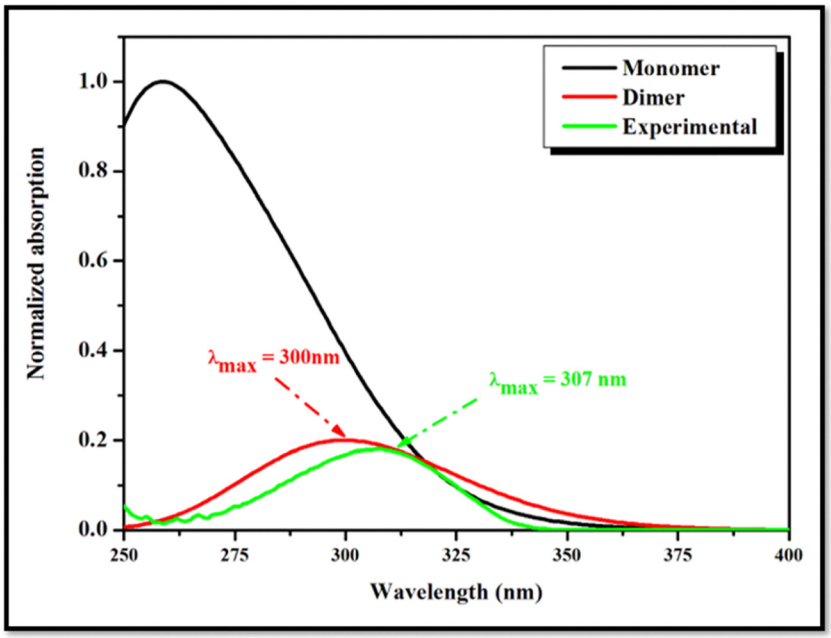

Fig. 9 TD-DFT validation of the experimental UV-visible spectra of the $(C_6H_9N_2)_2CdI_4$ compound: monomer and dimer absorption.

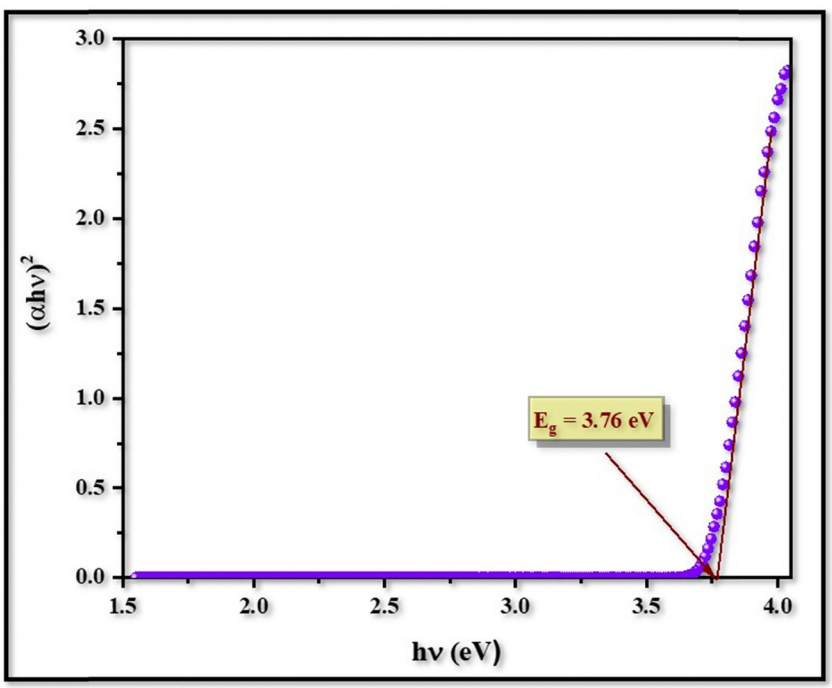

Fig. 10 Tauc plot for $(C_6H_9N_2)_2CdI_4$.

The Gaussian 09[64] program was employed in these calculations within the IEFPCM solvation model[65] using water as solvent. Both the monomer and dimer absorption spectra of the investigated compound $(C_6H_9N_2)_2CdI_4$ were computed using the TD-B3LYP-D3/LanL2DZ level of theory.[66,67] The calculated absorption spectra are depicted in Fig. 9, together with the experimental spectrum, and a significant correlation between the calculated and experimental data can be noticed. In addition to the monomer, the dimeric form was considered to account for possible intermolecular interactions (such as hydrogen bonding and halogen bridging) that can persist in solution and strongly influence the electronic structure. Compared to the monomer, the dimer showed a red-shifted absorption peak. This red shift reflects the impact of intermolecular interactions on the electronic

Table 6 Band gap energies for $(C_6H_9N_2)_2CdI_4$ compared to those reported in previous works

Compound	Band gap E_g (eV)	Ref.
$(C_6H_9N_2)_2CdCl_4$	3.43	29
$(C_6H_9N_2)_2CoCl_4$	3.47	27
$(C_6H_9N_2)FeCl_4$	2.47	30
$(C_6H_9N_2)_2MnI_4$	2.21	26
$(C_6H_9N_2)_2MnBr_4$	2.38	28
$(C_6H_9N_2)_2CdI_4$	3.76	This work

structure and provides a better match with the experimental data. Indeed, the dimer's maximum absorption wavelength (300 nm) is close to the experimental value of 307 nm, supporting the idea that aggregated species may coexist with monomers in solution.

Table 7 lists the major electronic transitions for the first three excited states that contributed to the absorption spectra for both the dimer and the monomer. The dimer transition analysis demonstrated that the HOMO → LUMO transition occurs at 340.21 nm with a low oscillator strength (0.0003).

HOMO and LUMO orbitals for the monomer and dimer of the studied compound were analyzed to gain insight into its electronic characteristics. The isosurfaces of the frontier molecular orbitals (FMOs) are shown in Fig. 11, highlighting the features of a π-conjugated system. The LUMO is delocalized over the acceptor group, corresponding to the organic moiety, for both the monomer and the dimer, whereas the HOMO is mainly concentrated on the donor core, represented by the inorganic CdI_4 group. For the monomer, the calculated HOMO and LUMO energy levels are −6.26 eV and −2.02 eV, respectively, and for the dimer, they are −5.98 eV and −2.01 eV. The HOMO–LUMO gap decreases slightly from 4.23 eV for the monomer to 3.97 eV for the dimer, suggesting enhanced conjugation and a tendency toward red-shifted optical properties. To provide more insight into the reactivity of the compound under investigation, a series of global chemical reactivity descriptors, including global hardness (η), chemical potential (μ), and global electrophilicity index values (ω), have been derived through the use of the HOMO and the LUMO energy values. These parameters are a nice way to show how chemical reactivity and structural strength are related. The equations listed below specify these parameters:[30,32,68]

$$\eta = \frac{E_{LUMO} - E_{HOMO}}{2} \quad (6)$$

$$\mu = \frac{E_{LUMO} + E_{HOMO}}{2} \quad (7)$$

and

$$\omega = \frac{\mu^2}{2\eta} \quad (8)$$

The simulated values of global hardness, chemical potential, and electrophilicity index are 1.98 eV, −3.99 eV, and 4.01 eV, respectively (Table 8). These indicate moderate electronic kinetic stability (high η, low polarizability) and a propensity for intramolecular charge transfer from the electron-rich organic cation (higher-lying HOMO) to the $[CdI_4]^{2-}$ acceptor unit (moderate ω), consistent with the TD-DFT transition analysis. The negative chemical potential confirms the overall thermodynamic stability of the dimer.

To investigate the nature of the intermolecular interactions and the non-covalent interactions in the $(C_6H_9N_2)_2CdI_4$ compound, we investigated the reduced density gradient (RDG) for the dimer system.[69–71] Multiwfn[72] software was employed to do the RDG computations, enabling the extraction of the electron density and the gradient data from the calculated wavefunction. The VMD[73] program was then used to present the RDG isosurfaces. Distinct peaks in the RDG profile were found by the RDG analysis of the $(C_6H_9N_2)_2CdI_4$ dimer, indicating the presence of several intermolecular interactions that control the system's stability (see Fig. 12). However, significant peaks linked to hydrogen bonding were seen between the iodine atoms of the CdI_4 unit and the nitrogen atoms of the $(C_6H_9N_2)_2$ groups. This interaction was shown as a blue area on the RDG isosurface, indicating strong attractive forces that play a major role in stabilizing the structure. Furthermore, weaker van der Waals interactions have been observed, as shown by green-colored RDG areas. These dispersion forces between the organic and the inorganic components further stabilize the studied compound. Regions of strong repulsion were also detected; these were identified by red RDG areas that suggested steric hindrance or unfavorable spatial arrangements. The RDG analysis reveals a delicate equilibrium between these interactions, where steric repulsion affects the system's spatial arrangement while hydrogen bonding and van der Waals forces maintain it. The importance of non-covalent interactions in supporting the dimer's stability and structural integrity is shown by this detailed investigation.

Table 7 Simulated absorption wavelengths, excitation energies, oscillator strengths, and major contributions for monomer and dimer compounds, using TD-B3LYP-D3/LanL2DZ level of theory in water as solvent

Compound	Excited state	Wavelength (nm)	Energy (cm^{-1})	f	MO contributions
Monomer	S1	328.40	30450.87	0.0008	H → L+1 (59%)
	S2	328.02	30486.35	0.0001	H−1 → L (45%)
	S3	324.75	30792.85	0.0013	H−1 → L+1 (45%)
Dimer	S1	340.21	29393.47	0.0003	H → L (89%)
	S2	340.12	29401.53	0.0014	H → L+1 (91%)
	S3	338.76	29519.29	0.0007	H → L+2 (88%)

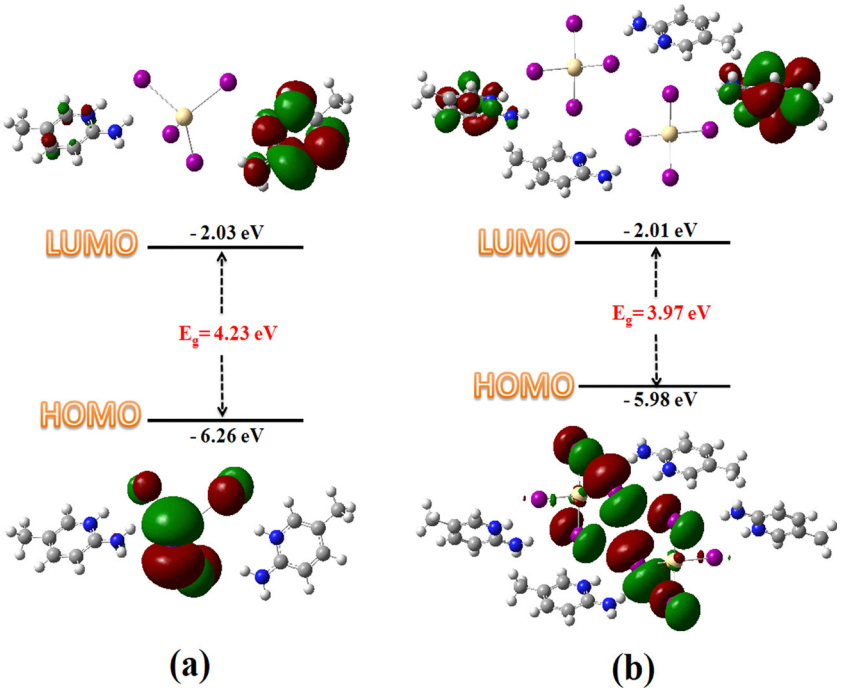

Fig. 11 The molecular frontier orbitals HOMO and LUMO computed with TD/B3LYP-D3/LANL2DZ method in water as solvent of the monomer (a) and the dimer (b) units for the studied compound $(C_6H_9N_2)_2CdI_4$.

Table 8 Global chemical reactivity descriptors for the dimer structure of the $(C_6H_9N_2)_2CdI_4$ compound, calculated at the TD-B3LYP-D3/LanL2DZ level of theory

Parameters	Values
E_{HOMO} (eV)	−5.98
E_{LUMO} (eV)	−2.01
HOMO–LUMO gap (eV)	3.97
Chemical potential (eV)	−3.99
Global hardness (eV)	1.98
Electrophilicity index (eV)	4.01

6. Evaluation of *in vitro* biological activity

Oxidative stress, arising from the excessive generation of reactive oxygen species (ROS) during normal metabolic processes, is known to cause severe damage to biological systems through lipid peroxidation, protein modification, and activation of stress-related signaling pathways. Antioxidants play a vital protective role by neutralizing free radicals through the donation of electrons or hydrogen atoms, thereby preventing the propagation of oxidative chain reactions.[74,75] In view of the growing interest in developing effective antioxidant materials, the antioxidant potential of the $(C_6H_9N_2)_2CdI_4$ compound was systematically assessed using complementary *in vitro* assays.

The free radical scavenging ability of $(C_6H_9N_2)_2CdI_4$ was first evaluated using the DPPH assay, a widely employed method based on the reduction of the stable nitrogen-centered DPPH radical (Fig. 13). The scavenging activity increased steadily with concentration, demonstrating a clear dose-dependent response. At a final concentration of 1 mg ml^{-1}, the compound exhibited approximately 60% radical scavenging efficiency,

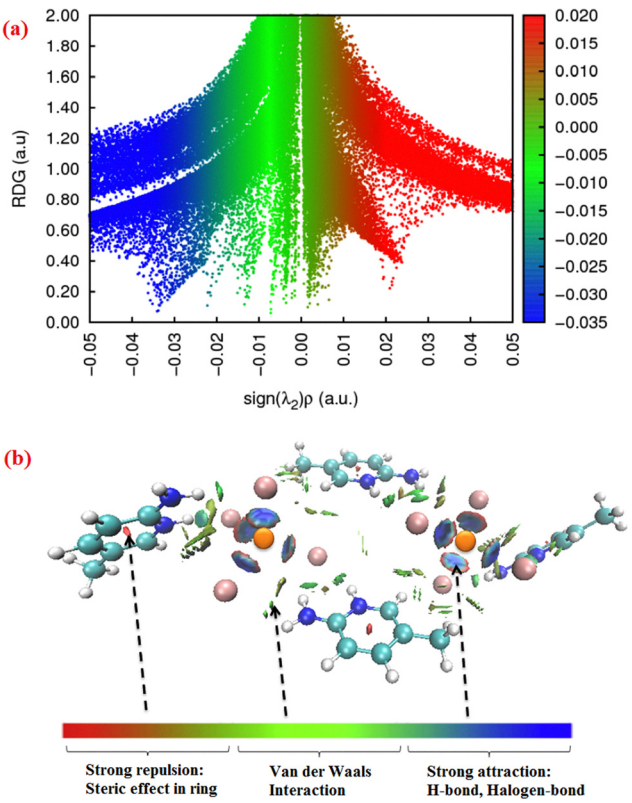

Fig. 12 RDG graph (a) and isosurface plot (b) of the $(C_6H_9N_2)_2CdI_4$ compound.

indicating its strong capacity to quench free radicals and interrupt radical chain reactions. This behavior suggests that

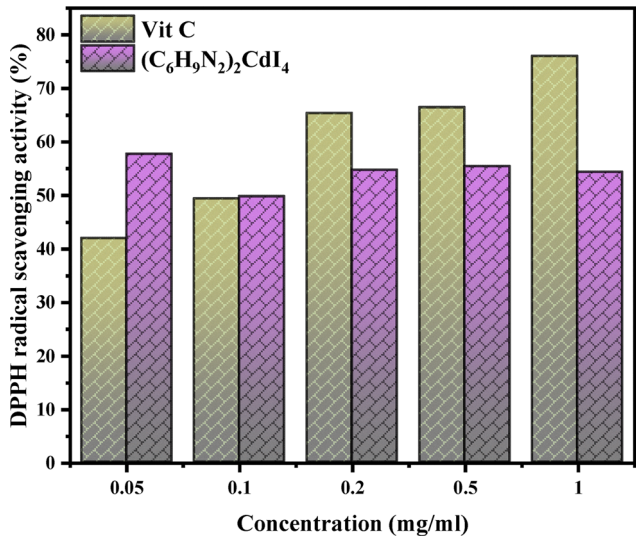

Fig. 13 DPPH radical scavenging activity of $(C_6H_9N_2)_2CdI_4$ at different concentrations.

$(C_6H_9N_2)_2CdI_4$ can effectively delay the onset of lipid oxidation, highlighting its potential as a promising antioxidant agent.

To further elucidate the antioxidant mechanism, the reducing power of $(C_6H_9N_2)_2CdI_4$ was investigated through the Fe^{3+}/ferricyanide reduction assay. This method evaluates the electron-donating ability of antioxidant compounds by monitoring the conversion of Fe^{3+} to Fe^{2+}. As shown in Fig. 14, the reducing power of the compound increased markedly with increasing concentration, reaching a maximum absorbance of approximately 0.7 at 700 nm for a concentration of 1 mg ml^{-1}.

The results obtained from both assays reveal a consistent antioxidant behavior, in which $(C_6H_9N_2)_2CdI_4$ acts as a reductone by donating electrons or hydrogen atoms to stabilize reactive species. The close agreement between the DPPH scavenging activity and the reducing power measurements further supports the existence of a direct correlation between antioxidant efficiency and electron-donating capability. Moreover, the enhanced activity observed may be attributed to the synergistic interaction between the organic ligand and the bismuth-iodide inorganic framework, which likely facilitates charge transfer processes. Overall, these findings demonstrate that $(C_6H_9N_2)_2CdI_4$ exhibits significant antioxidant potential, making it a suitable candidate for further investigation in antioxidant-related applications.

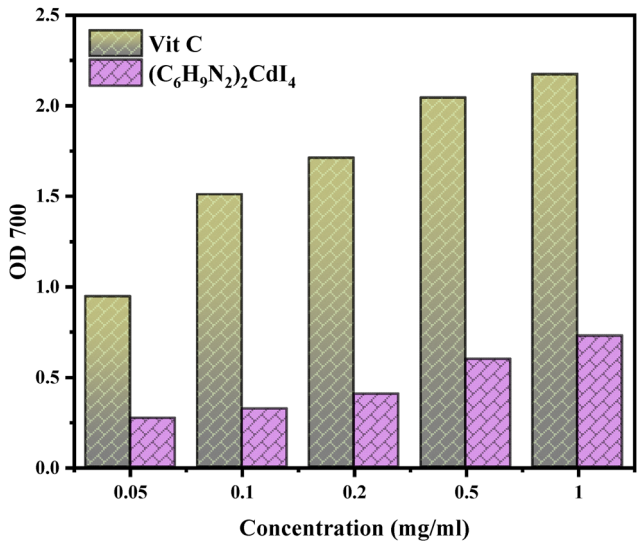

Fig. 14 Reducing power effect of $(C_6H_9N_2)_2CdI_4$ at different concentrations.

IV. Conclusion

The hybrid organic–inorganic compound $(C_6H_9N_2)_2CdI_4$ was successfully synthesized and thoroughly characterized through complementary experimental and computational approaches. Single-crystal X-ray diffraction revealed a triclinic structure comprising discrete $[CdI_4]^{2-}$ tetrahedra stabilized by extensive N–H···I hydrogen bonds, π-stacking interactions, and van der Waals contacts between protonated 2-amino-5-picolinium cations and inorganic anions, as confirmed by RDG/NCIPLOT analysis. Raman spectroscopy verified the characteristic Cd–I stretching modes, while SEM/EDX demonstrated compositional purity and homogeneous elemental distribution.

Optical measurements established a direct-allowed bandgap of 3.76 eV with a sharp $\pi \rightarrow \pi^*$ absorption edge at 307 nm attributable to the aromatic cation, validated by TD-DFT calculations on the dimer model. The wide bandgap, absence of low-energy d–d transitions, and minimal orbital overlap between isolated tetrahedra suggest low exciton binding energy suitable for UV optoelectronics. TGA/DSC analysis confirmed exceptional thermal stability with no mass loss or endothermic events up to 350 °C, substantially exceeding typical hybrid perovskites and enabling thin-film processing.

The compound also exhibited potent *in vitro* antioxidant activity, achieving 60% DPPH radical scavenging efficiency at 1 mg ml^{-1} and strong ferric reducing power, reflecting synergistic electron/hydrogen donation from the electron-rich organic ligand and redox-accessible CdI_4^{2-} framework. These combined properties, wide-bandgap semiconductivity, high thermal robustness, validated electronic structure, and biological activity, position $(C_6H_9N_2)_2CdI_4$ as a promising multifunctional material for UV photodetection, transparent electronics, and antioxidant applications.

Author contributions

Arafet Ghoudi: writing – original draft, validation, software, methodology, investigation. Walid Taouali: writing – original draft, validation, software, methodology, investigation. José A. Paixão: writing – original draft, visualization, formal analysis. Noweir Ahmad Alghamdi. formal analysis, validation, writing review. Rui Fausto: writing – review & editing, visualization, validation. Abderrazek Oueslati: writing – review & editing, visualization, validation, investigation, formal analysis, data curation.

Conflicts of interest

The authors declare that they have no known competing financial interests or personal relationships that could have appeared to influence the work reported in this paper.

Data availability

The authors confirm that the data used to support the findings of this study are included within the article and are available from the corresponding author upon reasonable request.

CCDC 2284327 contains the supplementary crystallographic data for this paper.[76]

References

1 G. A. Jeffrey, *An Introduction to Hydrogen Bonding*, Oxford University Press, 1997.
2 T. F. Headen, C. A. Howard and N. T. Skipper, *et al.*, Structure of π–π Interactions in Aromatic Liquids, *J. Am. Chem. Soc.*, 2010, **132**, 5735–5742, DOI: 10.1021/ja909084e.
3 F. Élie, *Liaison hydrogène et autres liaisons chimiques*, 2004.
4 T. Steiner, The Hydrogen Bond in the Solid State, *Angew. Chem., Int. Ed.*, 2002, **41**, 48–76, DOI: 10.1002/1521-3773(20020104)41:1%253C48::AID-ANIE48%253E3.0.CO;2-U.
5 C. Fonseca Guerra, F. M. Bickelhaupt, J. G. Snijders and E. J. Baerends, Hydrogen Bonding in DNA Base Pairs: Reconciliation of Theory and Experiment, *J. Am. Chem. Soc.*, 2000, **122**, 4117–4128, DOI: 10.1021/ja993262d.
6 A. R. Fersht, The hydrogen bond in molecular recognition, *Trends Biochem. Sci.*, 1987, **12**, 301–304, DOI: 10.1016/0968-0004(87)90146-0.
7 S. Selvakumari, C. Venkataraju and S. Muthu, *et al.*, Spectroscopic (FT-IR, FT-Raman, UV-Visible), Quantum Mechanical Based Computational Studies and Molecular Docking Analysis of 2-Amino-3,5-dichloropyridine, *Anal. Chem. Lett.*, 2021, **11**, 848–861, DOI: 10.1080/22297928.2021.1981440.
8 A. Rayes, M. Moncer and I. Ara, *et al.*, Synthesis, crystal structures, Hirshfeld surface analysis and physico-chemical characterization of two new ZnII and CdII halidometallates, *J. Mater. Sci.: Mater. Electron.*, 2021, **32**, 10890–10905, DOI: 10.1007/s10854-021-05747-3.
9 S. Selvakumari, C. Venkataraju and S. Muthu, *et al.*, Donor acceptor groups effect, polar protic solvents influence on electronic properties and reactivity of 2-Chloropyridine-4-carboxylic acid, *J. Indian Chem. Soc.*, 2022, **99**, 100478, DOI: 10.1016/j.jics.2022.100478.
10 S. Chongdar, S. Bhattacharjee, P. Bhanja and A. Bhaumik, Porous organic–inorganic hybrid materials for catalysis, energy and environmental applications, *Chem. Commun.*, 2022, **58**, 3429–3460, DOI: 10.1039/D1CC06340E.
11 W. Al Zoubi, D. K. Yoon, Y. G. Kim and Y. G. Ko, Fabrication of organic-inorganic hybrid materials on metal surface for optimizing electrochemical performance, *J. Colloid Interface Sci.*, 2020, **573**, 31–44, DOI: 10.1016/j.jcis.2020.03.117.
12 H. Ben Attia, F. Bentahar and M. S. M. Abdelbaky, *et al.*, Phase transitions, thermal, vibrational (FT-IR and Raman) and optical characterizations, dielectric relaxation and electrical conductivity of a cobalt(II) based hybrid material, *J. Alloys Compd.*, 2023, **969**, 172317, DOI: 10.1016/j.jallcom.2023.172317.
13 M. Catauro and S. Vecchio Ciprioti, Sol–Gel Synthesis and Characterization of Hybrid Materials for Biomedical Applications, in *Thermodynamics and Biophysics of Biomedical Nanosystems: Applications and Practical Considerations*, ed. C. Demetzos and N. Pippa. Springer, Singapore, 2019, pp. 445–475.
14 G. Voicu, R.-E. Geanaliu-Nicolae and A.-A. Pîrvan, *et al.*, Synthesis, characterization and bioevaluation of drug-collagen hybrid materials for biomedical applications, *Int. J. Pharm.*, 2016, **510**, 474–484, DOI: 10.1016/j.ijpharm.2015.11.054.
15 G. Sun, D. Chen, G. Zhu and Q. Li, Lightweight hybrid materials and structures for energy absorption: A state-of-the-art review and outlook, *Thin Wall Struct.*, 2022, **172**, 108760, DOI: 10.1016/j.tws.2021.108760.
16 A. Behera, A. K. Sahoo and S. S. Mohapatra, 14 – Nickel–titanium smart hybrid materials for automotive industry, in *Nickel-Titanium Smart Hybrid Materials*, ed. S. Thomas, A. Behera and T. A. Nguyen, Elsevier, 2022, pp. 271–295.
17 J. Liu, X. Chen, H. Yang and K. Shan, Hybrid renewable energy applications in zero-energy buildings and communities integrating battery and hydrogen vehicle storage, *Appl. Energy*, 2021, **290**, 116733, DOI: 10.1016/j.apenergy.2021.116733.
18 M. Alktranee and P. Bencs, Overview of the hybrid solar system, *Analecta Technica Szegedinensia*, 2020, **14**, 100–108, DOI: 10.14232/analecta.2020.1.100-108.
19 S. Bousalem, F. Z. Zeggai, H. Baltach and A. Benyoucef, Physical and electrochemical investigations on hybrid materials synthesized by polyaniline with various amounts of ZnO nanoparticle, *Chem. Phys. Lett.*, 2020, **741**, 137095, DOI: 10.1016/j.cplett.2020.137095.
20 S. M. Zachariah, Y. Grohens, N. Kalarikkal and S. Thomas, Hybrid materials for electromagnetic shielding: a review, *Polym. Compos.*, 2022, **43**, 2507–2544, DOI: 10.1002/pc.26595.
21 F. Yang and A. Wang, Recent researches on antimicrobial nanocomposite and hybrid materials based on sepiolite and palygorskite, *Appl. Clay Sci.*, 2022, **219**, 106454, DOI: 10.1016/j.clay.2022.106454.
22 N. Karâa, A. Ben Ahmed and B. Hamdi, New semiconductor halocadmate $[Cd_nX_m]_{(2n-m)}$ crystal structure, molecular conformation and theoretical investigations, *J. Solid State Chem.*, 2023, **322**, 123954, DOI: 10.1016/j.jssc.2023.123954.
23 J. A. Bis and M. J. Zaworotko, The 2-Aminopyridinium-carboxylate Supramolecular Heterosynthon: A Robust Motif for Generation of Multiple-Component Crystals, *Cryst. Growth Des.*, 2005, **5**, 1169–1179, DOI: 10.1021/cg049622c.
24 A. Fatima, M. Singh and K. M. Abualnaja, *et al.*, Experimental Spectroscopic, Structural (Monomer and Dimer), Molecular Docking, Molecular Dynamics Simulation and

Hirshfeld Surface Analysis of 2-Amino-6-Methylpyridine, *Polycyclic Aromat. Compd.*, 2023, **43**, 3910–3940, DOI: 10.1080/10406638.2022.2080726.

25 N. Kavitha and M. Alivelu, The Computational Study, 3D-QSAR, and Molecular Docking Study of 2-Amino 5-Methyl Pyridine, *Polycyclic Aromat. Compd.*, 2023, **43**, 1495–1508, DOI: 10.1080/10406638.2022.2028871.

26 X. Wei, J. He and Y. Zhu, *et al.*, Synthesis, structure, and photoelectric properties of a novel zero-dimensional organic-inorganic hybrid perovskite $(C_6H_9N_2)_2MnI_4$, *Opt. Mater.*, 2023, **136**, 113360, DOI: 10.1016/j.optmat.2022.113360.

27 A. Ghoudi, I. Chaabane and R. Naouari, *et al.*, Optical and electric properties of the organic-inorganic hybrid bis(2-amino-5-picolinium) Tetrachlorocobaltate(II) $[(C_6H_9N_2)_2CoCl_4]$, *Inorg. Chem. Commun.*, 2024, **168**, 112925, DOI: 10.1016/j.inoche.2024.112925.

28 J. He, H. Zhao and X. Hu, *et al.*, Synthesis, Structure, and Photoelectric Properties of a Novel 0-Dimensional Organic–Inorganic Hybrid Perovskite $(2\text{-}5\text{-}py)_2MnBr_4$, *J. Phys. Chem. C*, 2021, **125**, 22898–22906, DOI: 10.1021/acs.jpcc.1c07221.

29 I. Jomaa, F. Bardak and N. Issaoui, *et al.*, Synthesis of 2-amino-5-methylpyridinium tetrachloridocadmate(II) $(C_6H_9N_2)_2[CdCl_4]$: structure, DFT-calculated descriptors and molecular docking study, *J. King Saud Univ., Sci.*, 2024, **36**, 103178, DOI: 10.1016/j.jksus.2024.103178.

30 A. Ghoudi, K. B. Brahim and H. Ghalla, *et al.*, Crystal structure and optical characterization of a new hybrid compound, $C_6H_9N_2FeCl_4$, with large dielectric constants for field-effect transistors, *RSC Adv.*, 2023, **13**, 12844–12862, DOI: 10.1039/D3RA01239E.

31 I. Chaabane, W. Rekik and M. Zaghrioui, *et al.*, Synthesis, crystal structure, and ionic conductivity of a new organic–inorganic bromides $(C_6H_9N_2)_2[SbBr_4]Br$, *Ionics*, 2024, **30**, 5827–5844, DOI: 10.1007/s11581-024-05680-5.

32 I. Chaabane, W. Rekik and H. Ghalla, *et al.*, Crystal structure, optical characterization, conduction and relaxation mechanisms of a new hybrid compound $(C_6H_9N_2)_2[Sb_2Cl_8]$, *RSC Adv.*, 2024, **14**, 3588–3598, DOI: 10.1039/D3RA08885E.

33 I. Garoui, S. Hajlaoui and I. Kammoun, *et al.*, Synthesis, crystal structure, BFDH morphology, Hirshfeld surface analysis and electrical characterization of the new bi-(2-amino-5-methylpyridinium) hexa-chlorostannate compound, *Phys. E*, 2024, **158**, 115897, DOI: 10.1016/j.physe.2024.115897.

34 A. S. Albrecht, C. P. Landee and M. M. Turnbull, Structure of bis(2-amino-5-methylpyridinium) tetrachlorozincate at 298 and 150 K, *J. Chem. Crystallogr.*, 2003, **33**, 269–276, DOI: 10.1023/A:1023829127254.

35 S. Bruker and S. Saint, Bruker AXS Inc., Madison, Wisconsin, USA, 2002.

36 G. M. Sheldrick, *SADABS*, Bruker AXS Inc., Madison, Wisconsin, USA, 2002, Acta Crystallographica Section E Structure Reports Online ISSN 1600–5368.

37 L. J. Farrugia, WinGX suite for small-molecule single-crystal crystallography, *J. Appl. Crystallogr.*, 1999, **32**, 837–838, DOI: 10.1107/S0021889899006020.

38 P. Bersuder, M. Hole and G. Smith, Antioxidants from a heated histidine-glucose model system. I: investigation of the antioxidant role of histidine and isolation of antioxidants by high-performance liquid chromatography, *J. Am. Oil Chem. Soc.*, 1998, **75**, 181–187, DOI: 10.1007/s11746-998-0030-y.

39 A. Yıldırım, A. Mavi and A. A. Kara, Determination of Antioxidant and Antimicrobial Activities of Rumex crispus L. Extracts, *J. Agric. Food Chem.*, 2001, **49**, 4083–4089, DOI: 10.1021/jf0103572.

40 H.-Y. Wu, C.-L. Hu and M.-B. Xu, *et al.*, From $H_{12}C_4N_2CdI_4$ to $H_{11}C_4N_2CdI_3$: a highly polarizable CdNI 3 tetrahedron induced a sharp enhancement of second harmonic generation response and birefringence, *Chem. Sci.*, 2023, **14**, 9533–9542, DOI: 10.1039/D3SC03052K.

41 W. H. Baur, The geometry of polyhedral distortions. Predictive relationships for the phosphate group, *Acta Crystallogr., Sect. B*, 1974, **30**, 1195–1215, DOI: 10.1107/S0567740874004560.

42 L. Yang, D. R. Powell and R. P. Houser, Structural variation in copper(I) complexes with pyridylmethylamide ligands: structural analysis with a new four-coordinate geometry index, τ_4, *Dalton Trans.*, 2007, 955–964, DOI: 10.1039/B617136B.

43 C. Janiak, A critical account on π–π stacking in metal complexes with aromatic nitrogen-containing ligands, *J. Chem. Soc., Dalton Trans.*, 2000, 3885–3896, DOI: 10.1039/B003010O.

44 N. J. Singh, S. K. Min, D. Y. Kim and K. S. Kim, Comprehensive Energy Analysis for Various Types of π-Interaction, *J. Chem. Theory Comput.*, 2009, **5**, 515–529, DOI: 10.1021/ct800471b.

45 M. Javed, A. Arif Khan and J. Kazmi, *et al.*, Investigation on electrical transport and dielectric relaxation mechanism in TbCrO3 perovskite orthochromite, *J. Alloys Compd.*, 2023, **955**, 170181, DOI: 10.1016/j.jallcom.2023.170181.

46 R. Sudharsanan, T. K. K. Srinivasan and S. Radhakrishna, Raman and far IR studies on Ag_2CdI_4 and Cu_2CdI_4 superionic compounds, *Solid State Ionics*, 1984, **13**, 277–283, DOI: 10.1016/0167-2738(84)90069-9.

47 L. Zhang, J. Wang and F. Han, *et al.*, Crystal structure and electrical conduction of the new organic-inorganic compound $(CH_2)_2(NH_3)_2CdI_4$, *J. Mol. Struct.*, 2018, **1156**, 450–456, DOI: 10.1016/j.molstruc.2017.11.130.

48 A. Kessentini, M. Belhouchet and J. J. Suñol, *et al.*, Synthesis, crystal structure, vibrational spectra, optical properties and theoretical investigation of bis(2-aminobenzimidazolium) tetraiodocadmate, *J. Mol. Struct.*, 2013, **1039**, 207–213, DOI: 10.1016/j.molstruc.2013.02.006.

49 M. Ghanbari, S. Gholamrezaei and M. Salavati-Niasari, Ag_2CdI_4: synthesis, characterization and investigation the strain lattice and grain size, *J. Alloys Compd.*, 2016, **667**, 115–122, DOI: 10.1016/j.jallcom.2016.01.085.

50 M. Tahenti, S. Gatfaoui and N. Issaoui, *et al.*, A tetrachlorocobaltate(II) salt with 2-amino-5-picolinium: Synthesis, theoretical and experimental characterization, *J. Mol.*

Struct., 2020, **1207**, 127781, DOI: 10.1016/j.molstruc.2020.127781.

51 T.-D. Kim and K.-S. Lee, D–π–A Conjugated Molecules for Optoelectronic Applications, *Macromol. Rapid Commun.*, 2015, **36**, 943–958, DOI: 10.1002/marc.201400749.

52 S. A. Khan, F. S. Al-Hazmi and S. Al-Heniti, *et al.*, Effect of cadmium addition on the optical constants of thermally evaporated amorphous Se–S–Cd thin films, *Curr. Appl. Phys.*, 2010, **10**, 145–152, DOI: 10.1016/j.cap.2009.05.010.

53 J. Lv, M. Xu and S. Lin, *et al.*, Direct-gap semiconducting trilayer silicene with 29% photovoltaic efficiency, *Nano Energy*, 2018, **51**, 489–495, DOI: 10.1016/j.nanoen.2018.06.079.

54 N. Kobayashi, H. Kuwae and J. Oshima, *et al.*, A wide-energy-gap naphthalene-based liquid organic semiconductor host for liquid deep-blue organic light-emitting diodes, *J. Lumin.*, 2018, **200**, 19–23, DOI: 10.1016/j.jlumin.2018.03.072.

55 S. Liu, L. He and Y. Wang, *et al.*, Tunable phase transition, band gap and SHG properties by halogen replacement of hybrid perovskites [(thiomorpholinium)PbX_3, X = Cl, Br, I], *Chin. Chem. Lett.*, 2022, **33**, 1032–1036, DOI: 10.1016/j.cclet.2021.07.039.

56 S. Meloni, G. Palermo and N. Ashari-Astani, *et al.*, Valence and conduction band tuning in halide perovskites for solar cell applications, *J. Mater. Chem. A*, 2016, **4**, 15997–16002, DOI: 10.1039/C6TA04949D.

57 R. P. Matthews, C. Ashworth, T. Welton and P. A. Hunt, The impact of anion electronic structure: similarities and differences in imidazolium based ionic liquids, *J. Phys.: Condens. Matter*, 2014, **26**, 284112, DOI: 10.1088/0953-8984/26/28/284112.

58 H. Y. Zhang, Z. L. Zhang and K. Q. Ye, *et al.*, Organic Crystals with Tunable Emission Colors Based on a Single Organic Molecule and Different Molecular Packing Structures, *Adv. Mater.*, 2006, **18**, 2369–2372, DOI: 10.1002/adma.200600704.

59 A. Thatribud and A. Rassamesard, Electronic and optical properties of lead halide perovskite ($MAPbX_3$) (X = I, Br, and Cl) by first principles calculations, *Phys. Scr.*, 2022, **97**, 055818, DOI: 10.1088/1402-4896/ac6543.

60 E. Mosconi, P. Umari and F. D. Angelis, Electronic and optical properties of $MAPbX_3$ perovskites (X = I, Br, Cl): a unified DFT and GW theoretical analysis, *Phys. Chem. Chem. Phys.*, 2016, **18**, 27158–27164, DOI: 10.1039/C6CP03969C.

61 S. Wang, H. Zhu and M. Sheng, *et al.*, Advances of Low-Dimensional Organic-Inorganic Hybrid Metal Halide Luminescent Materials: A Review, *Crystals*, 2025, **15**, 364, DOI: 10.3390/cryst15040364.

62 A. S. Berezin, M. P. Davydova and D. G. Samsonenko, *et al.*, A family of brightly emissive homo- and mixed-halomanganates(II): the effect of halide on optical and magnetic properties, *J. Lumin.*, 2021, **236**, 118069, DOI: 10.1016/j.jlumin.2021.118069.

63 T. K. Dennington and J. Millam, *GaussView, Version 5*, Semichem Inc., Shawnee Mission, KS, 2009. 31Spartan'8, Wavefunction. Inc, Irvine, CA, 2009.

64 M. J. E. A. Frisch, *Gaussian 09, Revision d.01*, Gaussian Inc., Wallingford CT 201, 2009.

65 E. Cancès, B. Mennucci and J. Tomasi, A new integral equation formalism for the polarizable continuum model: Theoretical background and applications to isotropic and anisotropic dielectrics, *J. Chem. Phys.*, 1997, **107**, 3032–3041, DOI: 10.1063/1.474659.

66 A. D. Becke, Density-functional exchange-energy approximation with correct asymptotic behavior, *Phys. Rev. A: At., Mol., Opt. Phys.*, 1988, **38**, 3098–3100, DOI: 10.1103/PhysRevA.38.3098.

67 C. Lee, W. Yang and R. G. Parr, Development of the Colle-Salvetti correlation-energy formula into a functional of the electron density, *Phys. Rev. B: Condens. Matter Mater. Phys.*, 1988, **37**, 785–789, DOI: 10.1103/PhysRevB.37.785.

68 A. Ghoudi, S. Auguste and J. Lhoste, *et al.*, Crystal Structure and Spectroscopic Characterization of a New Hybrid Compound, $(C_{12}H_{17}N_2)_2[CdBr_4]$, for Energy Storage Applications, *ACS Omega*, 2024, **9**, 28339, DOI: 10.1021/acsomega.4c01997.

69 G. Saleh, C. Gatti, L. Lo Presti and J. Contreras-García, Revealing Non-covalent Interactions in Molecular Crystals through Their Experimental Electron Densities, *Chem. – Eur. J.*, 2012, **18**, 15523–15536, DOI: 10.1002/chem.201201290.

70 W. Taouali and K. Alimi, Optimizing non-fullerene acceptor molecules constituting fluorene core for enhanced performance in organic solar cells: a theoretical methodology, *J. Mol. Model.*, 2024, **30**, 342, DOI: 10.1007/s00894-024-06120-x.

71 J. Contreras-García, E. R. Johnson and S. Keinan, *et al.*, NCIPLOT: A Program for Plotting Noncovalent Interaction Regions, *J. Chem. Theory Comput.*, 2011, **7**, 625–632, DOI: 10.1021/ct100641a.

72 T. Lu and F. Chen, Multiwfn: a multifunctional wavefunction analyzer, *J. Comput. Chem.*, 2012, **33**, 580–592, DOI: 10.1002/jcc.22885.

73 W. Humphrey, A. Dalke and K. Schulten, VMD: Visual molecular dynamics, *J. Mol. Graphics*, 1996, **14**, 33–38, DOI: 10.1016/0263-7855(96)00018-5.

74 A. Feki, H. B. Saad and I. Bkhairia, *et al.*, Cardiotoxicity and myocardial infarction-associated DNA damage induced by thiamethoxam in vitro and in vivo: Protective role of Trigonella foenum-graecum seed-derived polysaccharide, *Environ. Toxicol.*, 2019, **34**, 271–282, DOI: 10.1002/tox.22682.

75 S. B. Ali, A. Feki and V. Ferretti, *et al.*, Crystal structure, spectroscopic measurement, optical properties, thermal studies and biological activities of a new hybrid material containing iodide anions of bismuth(III), *RSC Adv.*, 2020, **10**, 35174–35184, DOI: 10.1039/D0RA05646D.

76 CCDC 2284327: Experimental Crystal Structure Determination, 2026, DOI: 10.5517/ccdc.csd.cc2gp0z5.